The Astrophysical Journal, 914:30 (12pp), 2021 June 10 https://doi.org/10.3847/1538-4357/abf9a2

An 86 GHz Search for Pulsars in the Galactic Center with the Atacama Large Millimeter / submillimeter Array

Kuo Liu[1], Gregory Desvignes[1,2], Ralph P. Eatough[3,1], Ramesh Karuppusamy[1], Michael Kramer[1], Pablo Torne[1,4], Robert Wharton[1], Shami Chatterjee[5], James M. Cordes[5], Geoffrey B. Crew[6], Ciriaco Goddi[7,8], Scott M. Ransom[9], Helge Rottmann[1], Federico Abbate[1], Geoffrey C. Bower[10], Christiaan D. Brinkerink[7], Heino Falcke[7,1], Aristeidis Noutsos[1], Antonio Hernández-Gómez[1], Wu Jiang (江悟)[11,12], Michael D. Johnson[13,14], Ru-Sen Lu (路如森)[11,15,1], Yurii Pidopryhora[1], Luciano Rezzolla[16,17,18], Lijing Shao[15,1,19], Zhiqiang Shen (沈志强)[11,12], and Norbert Wex[1]

[1] Max-Planck-Institut für Radioastronomie, Auf dem Hügel 69, D-53121 Bonn, Germany; kliu@mpifr-bonn.mpg.de
[2] LESIA, Observatoire de Paris, Université PSL, CNRS, Sorbonne Université, Université de Paris, 5 place Jules Janssen, F-92195 Meudon, France
[3] National Astronomical Observatories, Chinese Academy of Sciences, 20A Datun Road, Chaoyang District, Beijing 100101, People's Republic of China
[4] Instituto de Radioastronomía Milimétrica, IRAM, Avenida Divina Pastora 7, Local 20, S-18012, Granada, Spain
[5] Cornell Center for Astrophysics and Planetary Science, Cornell University, Ithaca, NY 14853, USA
[6] Massachusetts Institute of Technology Haystack Observatory, 99 Millstone Road, Westford, MA 01886, USA
[7] Department of Astrophysics, Institute for Mathematics, Astrophysics and Particle Physics (IMAPP), Radboud University, P.O. Box 9010, 6500 GL Nijmegen, The Netherlands
[8] Leiden Observatory—Allegro, Leiden University, P.O. Box 9513, 2300 RA Leiden, The Netherlands
[9] National Radio Astronomy Observatory, Charlottesville, VA 22903, USA
[10] Institute of Astronomy and Astrophysics, Academia Sinica, 645 N. A'ohoku Place, Hilo, HI 96720, USA
[11] Shanghai Astronomical Observatory, Chinese Academy of Sciences, 80 Nandan Road, Shanghai 200030, People's Republic of China
[12] Key Laboratory of Radio Astronomy, Chinese Academy of Sciences, Nanjing 210008, People's Republic of China
[13] Center for Astrophysics | Harvard & Smithsonian, 60 Garden Street, Cambridge, MA 02138, USA
[14] Black Hole Initiative at Harvard University, 20 Garden Street, Cambridge, MA 02138, USA
[15] Kavli Institute for Astronomy and Astrophysics, Peking University, Beijing 100871, People's Republic of China
[16] Institut für Theoretische Physik, Max-von-Laue-Strasse 1, D-60438 Frankfurt, Germany
[17] Frankfurt Institute for Advanced Studies, Ruth-Moufang-Strasse 1, D-60438 Frankfurt, Germany
[18] School of Mathematics, Trinity College, Dublin 2, Ireland
[19] National Astronomical Observatories, Chinese Academy of Sciences, Beijing 100012, People's Republic of China
Received 2021 March 16; revised 2021 April 10; accepted 2021 April 18; published 2021 June 11

Abstract

We report on the first pulsar and transient survey of the Galactic Center (GC) with the Atacama Large Millimeter/submillimeter Array (ALMA). The observations were conducted during the Global Millimeter VLBI Array campaign in 2017 and 2018. We carry out searches using time series of both total intensity and other polarization components in the form of Stokes parameters. We incorporate acceleration and its derivative in the pulsar search, and also search in segments of the entire observation to compensate for potential orbital motion of the pulsar. While no new pulsar is found, our observations yield the polarization profile of the GC magnetar PSR J1745−2900 at millimeter wavelength for the first time, which turns out to be nearly 100% linearly polarized. Additionally, we estimate the survey sensitivity placed by both system and red noise, and evaluate its capability of finding pulsars in orbital motion with either Sgr A* or a binary companion. We show that the survey is sensitive to only the most luminous pulsars in the known population and future observations with ALMA in Band-1 will deliver significantly deeper survey sensitivity on the GC pulsar population.

Unified Astronomy Thesaurus concepts: Pulsars (1306); Radio pulsars (1353); Galactic center (565)

1. Introduction

The inner parsec of our Galaxy has been an exciting laboratory in particular for probing gravity in the past decades. This is mainly thanks to the Nobel-Prize-winning discovery of the supermassive black hole at the Galactic Center (GC) (Eckart & Genzel 1996; Ghez et al. 1998), whose corresponding radio source is known as Sgr A* (Krichbaum et al. 1993; Lo et al. 1993; Falcke et al. 2000; Plewa et al. 2015). Infrared observations have revealed that Sgr A* is surrounded by a dense group of orbiting young and old stars, commonly referred to as the S-star cluster (Eckart et al. 1993; Schödel et al. 2002; Ghez et al. 2003; Eisenhauer et al. 2005). Monitoring of the S stars has led to a precise determination of the mass of Sgr A* (Eckart & Genzel 1996; Ghez et al. 1998; Boehle et al. 2016; Gillessen et al. 2017) and recent measurements of gravitational redshift and Schwarzschild precession of the S2 star orbit (Gravity Collaboration et al. 2018, 2020; Do et al. 2019). Near-infrared and X-ray observations of flares occurring around Sgr A* imply a significant rotation of the supermassive black hole (Genzel et al. 2003; Aschenbach et al. 2004).

In parallel, radio imaging studies using very long baseline interferometry at millimeter wavelengths have demonstrated the compactness of Sgr A*, yielding an estimate on the intrinsic angular size of 40–60 μas, which corresponds to only 4–6 Schwarzschild radii (Doeleman et al. 2008; Fish et al. 2011; Johnson et al. 2018; Lu et al. 2018). These crude estimates are expected to soon be replaced by 1.3 mm images of Sgr A* with observations of the Event Horizon Telescope (Event Horizon Telescope Collaboration et al. 2019).

Pulsars in orbit around Sgr A*, once found, will allow follow-up pulsar timing observations that can yield estimates for the mass, spin, and possibly the quadrupole moment of Sgr A* with unprecedented precision (Wex & Kopeikin 1999; Kramer et al. 2004; Liu et al. 2012; Psaltis et al. 2016; Liu & Eatough 2017; De Laurentis et al. 2018). The assembly of all

aforementioned experiments will deliver a multimessenger experiment on gravity (Psaltis et al. 2016; Goddi et al. 2017), testing the fundamental principles in black hole physics of general relativity, e.g.., the cosmic censorship conjecture and no-hair theorem. Finding pulsars in the inner parsec will in addition provide a direct probe into the magnetoionized environment in the vicinity of Sgr A* and shed light on the structure of its accretion flows (Eatough et al. 2013b; Desvignes et al. 2018).

Starting in the 1990 s, pulsar searches toward the GC have so far discovered six radio-emitting neutron stars within half a degree from Sgr A* (Johnston et al. 2006; Deneva et al. 2009; Eatough et al. 2013b). The GC magnetar PSR J1745−2900, initially identified in an X-ray (Mori et al. 2013; Rea et al. 2013), is the only one out of the six inhabiting the innermost parsec. The number of discoveries is well below the substantial expected population of pulsars in the GC region (e.g., Pfahl & Loeb 2004; Wharton et al. 2012; Chennamangalam & Lorimer 2014; Zhang et al. 2014).

The main challenge of the searches at decimeter wavelengths, also summarized in Cordes & Lazio (1997), Macquart et al. (2010), Johnston et al. (2006), and Eatough et al. (2021, in preparation), is the high brightness temperature of the GC region (Reich et al. 1990) and the temporal scattering of the electromagnetic pulses when they propagate from the GC through the dense ionized interstellar medium (ISM) to the Earth. Though the GC magnetar PSR J1745−2900 exhibits much less temporal scattering than previously predicted (Spitler et al. 2014) and similar angular broadening as Sgr A* (Bower et al. 2014, 2015), it is still debatable whether one or a few lines of sight are representative given the spatial complexity of scattering materials in the GC (Lazio & Cordes 1998; Eatough et al. 2015). The combined angular and temporal broadening of PSR J1745−2900 suggest that the angular broadening is dominated by plasma far from Sgr A* (Bower et al. 2014). The scattering of the other GC pulsars also suggests a complex picture, with the material arising at multiple long distances from the GC (Dexter et al. 2017). Imaging observation of the extragalactic background source, G359.087+018, additionally supports the existence of patchy scattering structure in the GC (Lazio et al. 1999). Thus, strong scattering could still heavily affect the detectability of GC pulsars in low-frequency searches (Spitler et al. 2014; Macquart & Kanekar 2015), motivating searches at shorter wavelengths where temporal scattering ($\propto \lambda^4$) and the background noise of the GC is much less significant.

Very recently, Eatough et al. (2021, in preparation) and Torne et al. (2021) have reported pulsar search efforts at observing wavelengths ranging from 6 cm down to 2 mm. At these wavelengths, sensitivity becomes a more important limiting factor given that pulsars are typically steep-spectrum radio sources. Moreover, significant power baseline variation is commonly seen in observations at these wavelengths, as a result of fluctuation in the troposphere contribution to the overall system temperature (e.g., Liu et al. 2019). This effect is known to degrade de facto survey sensitivity, especially for long-period pulsars ($P \gtrsim 0.1s$) (Lazarus et al. 2015).

Therefore, for high-frequency surveys it is crucial to have highly sensitive facilities with relatively steady tropospheric weather conditions. In light of such, the Atacama Large Millimeter/submillimeter Array (ALMA) is an ideal instrument for pulsar searching in the GC. While normally being operated as an interferometer, ALMA can now also coherently combine individual antennas and form a tied-array beam toward a single pointing, which was developed under the ALMA Phasing Project (APP; Matthews et al. 2018). The ALMA phasing system currently allows a coherent addition of up to 50 (usually 41) 12 m antennas, which delivers a sensitivity equivalent to maximally a 84 m single dish at mm-wavelengths. The excellent site location and the feature of being an interferometer minimize the level of power baseline variation and guarantee the least possible radio interference (see e.g., the ALMA Technical Handbook[20]). Additionally, since pulsars are typically highly polarized radio sources, the assurance of polarization purity in the ALMA observations (Goddi et al. 2019), provides a complementary probe for the surveys as will be discussed below. Recently, a dedicated pulsar observing mode with the phased ALMA has been developed under the ALMA Pulsar Mode Project (APMP)[21], which demonstrates the strength and the quality of data with ALMA for pulsar studies (Liu et al. 2019).

In this paper, we report the first pulsar and transient search of the GC with ALMA. The paper is organized as follows. Section 2 describes details of the observations carried out. Results of the searches conducted can be found in Section 3. We further discuss the sensitivity of the survey in Section 4 and its effectiveness in probing the GC pulsar population in Section 5. A brief conclusion is presented in Section 6.

2. Observations and Data Processing

Observations of Sgr A* ($\alpha_{J2000} = 17^h45^m40^s.0361$, $\delta_{J2000} = -29°00'28''.168$) with ALMA were carried out at 3.5 mm during the Global Millimeter VLBI Array (GMVA) campaign on 2017 April 03 and 2018 April 14 and 17 (Issaoun et al. 2019, 2021, in preparation). The array was coherently combined using the phasing mode developed by the APP. The sky coverage of the resulting synthetic beams in these two campaigns is shown in Figure 1. At each epoch, the duration of the track was approximately 6 hr in total, and divided into individual scans of approximately 3−6 minutes each, switching between Sgr A* and calibrator sources that include 3C 279, NRAO 530, and J1924−2914 (OV −236). Baseband voltage data of 2 GHz bandwidth centered at 86.268 GHz were recorded in 2-bit samples on spinning disks in MARK 6 recorders with dual polarization. We refer to Goddi et al. 2019 for more details on phasing observations and data acquisition of ALMA.

The data on Sgr A* were later processed into intensity time series and written in PSRFITS format in search mode using the software tool `vdif2psrfits` developed under the APMP (Liu et al. 2019). The PSRFITS product contains time series of four Stokes parameters stored in 32 -bit float samples, with time and frequency resolutions of 8 μs and 62.5 MHz, respectively. Though the converted PSRFITS data did not proceed through the Level 2 Quality Assurance (QA2) stage for gain and leakage calibration, both are no more than a few percent for the observations (Goddi et al. 2019, 2021, in preparation). This means that the polarization of the data is trustworthy at a similar level of precision.

[20] https://almascience.eso.org/documents-and-tools/cycle8/alma-technical-handbook
[21] http://hosting.astro.cornell.edu/research/almapsr/

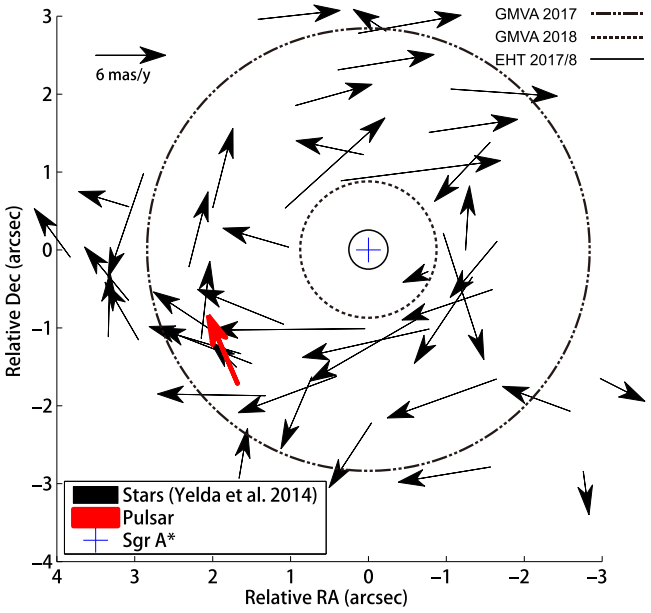

Figure 1. ALMA synthetic beams (full width at half maximum) in the GMVA 2017 and 2018 campaigns (at 86 GHz), along with that from the Event Horizon Telescope (EHT) 2017 and 2018 observations (at 228 GHz) as a comparison (Event Horizon Telescope Collaboration et al. 2019). The black arrows represent the position and the direction of motion of the S stars and the GC magnetar PSR J1745−2900 is marked by the red arrow. The size of the ALMA synthetic beam (in arcsec, $''$) is given by $\theta = 76''/(L_{\rm max} f)$ as given in the ALMA Technical Handbook, where $L_{\rm max}$ is the maximum baseline (in km) and f is the observing frequency (in GHz). For GMVA 2017, 2018 and EHT 2017/8 observations, $L_{\rm max}$ is 0.155, 0.5, and 0.46 km, respectively, which in turn gives $\theta \simeq 5\farcs7$, $1\farcs8$, and $0\farcs72$. This figure is based on a reproduction of Figure 3 in Bower et al. (2015).

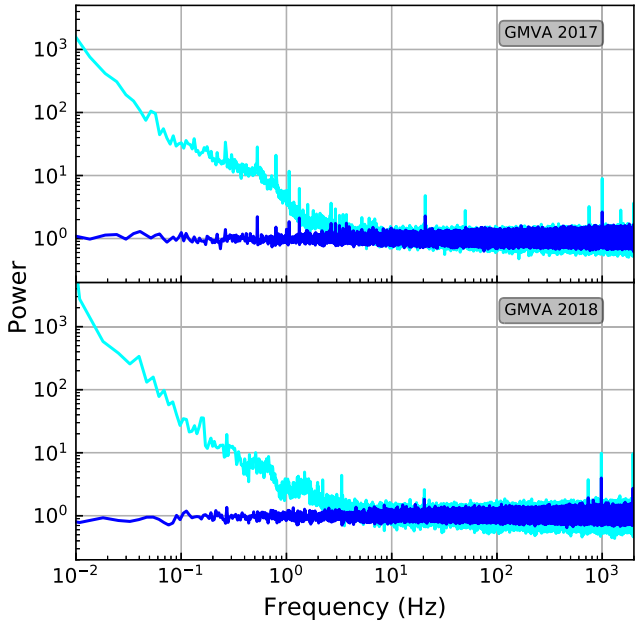

Figure 2. Fourier power spectrum of the total intensity data set from GMVA 2017 and 2018 campaigns, respectively, before (cyan) and after (blue) the application of spectrum whitening.

During the postprocessing, we noticed a power drop-off feature in the data, with a period of 18.192 s that coincides with the phasing cycle of the array (see Goddi et al. 2019, for details). We accordingly developed a dedicated scheme to mitigate this effect, which has significantly improved the data quality in terms of searching for time-domain signals. More details can be found in Appendix A. It was also found that the data recorded on 2018 April 14 were heavily affected by packet losses (up to 20% per scan for one polarization in a number of small chunks) during the data recording. Thus, we focused on data from 2017 April 03 and 2018 April 17 for the analysis in the rest of the paper.

3. Results

3.1. Periodicity Search

We searched for periodic signals in the data set using the Fourier-domain technique incorporated in the PRESTO software package (Ransom et al. 2002; Andersen & Ransom 2018). For each epoch, the time series from individual scans on the Sgr A* were coherently connected (with samples equal to the mean filled in the gaps), resampled to a time resolution of 32 μs, and dedispersed with a dispersion measure (DM) of 1700 cm^{-3} pc using PRESTO's `prepdata` program. The dedispersion corrects for the frequency-dependent time delay caused by the ISM along the line of sight, which, following Lorimer & Kramer (2005), can be calculated as

$$\delta\tau = 4.15\ {\rm ms} \times (f_{\rm low}^{-2} - f_{\rm high}^{-2}) \times {\rm DM} \quad (1)$$

where $f_{\rm low}$ and $f_{\rm high}$ are the low and high ends of the frequency band in units of GHz and $\delta\tau$ is in ms. The DM value was chosen based on the measurement of the GC magnetar PSR J1745−2900, which gave DM $\simeq$ 1770 cm^{-3} pc (Eatough et al. 2013b). The smearing time across the entire 2 GHz band centered at 86 GHz would be approximately 46 μs, slightly higher than our time resolution, if the dispersion delay were not compensated for. Subtracting a DM of 1700 cm^{-3} pc should therefore largely mitigate the DM smearing and leave the remaining part well below the sample interval for GC pulsars with DMs similar to that of PSR J1745−2900.

Power baseline variations are commonly seen in millimeter-wavelength observations as a consequence of system temperature fluctuations on timescales down to the order of seconds (Liu et al. 2019). This results in a reddening of the Fourier power spectrum and is already a known limiting factor to sensitivity in pulsar searches at longer wavelengths (e.g., Lazarus et al. 2015). To mitigate this impact in our data set, we used PRESTO's `rednoise` program to subtract a running median in the Fourier power spectrum before carrying out the search. The block size in Fourier frequency bins starts from six bins and is increased to 100 bins at a frequency of 10 Hz after which it remains constant. This has effectively whitened the Fourier power spectrum as shown in Figure 2, which subsequently improves the sensitivity of the search to slow pulsars (e.g., $P \gtrsim 0.1$ s).

We then used PRESTO's `accelsearch` program to search for periodicities in the data. To compensate for potential orbital motion of a pulsar, in addition to the spin period, we also varied the first and second period derivatives (acceleration and "jerk") to maximize sensitivity (e.g., Ransom et al. 2002; Bagchi et al. 2013; Eatough et al. 2013a). Here we considered two possible scenarios, a pulsar in orbit with Sgr A* or in a close binary system with another stellar-mass companion. For the former we used `accelsearch -zmax 1200 -wmax 40` and searched the full length of the data set, while for the latter we subdivided

Table 1
Number of Candidates Obtained from Both the Full-length and the Segmented Searches in the Timeseries of the Total Intensity and the Other Three Stokes Components in Total

Search	$N_{\rm I}$	$N_{Q,U,V}$
2017, full	153	61
2017, segments	2165	111
2018, full	217	84
2018, segments	2449	1693

the data set uniformly into three segments and used `accelsearch -zmax 1200 -wmax 1500` for each of the search individually. The segmented search provides additional sensitivity to pulsars in a compact orbit with a companion or in a close orbit with Sgr A* (e.g., Johnston & Kulkarni 1991). More details of the search sensitivity in terms of orbital motion for the applied options in `accelsearch` can be found in Section 4.2. We repeated the searches described above four times, using time series of the four Stokes parameters. The searches carried out in Q, U, and V (but not in $L = \sqrt{Q^2 + U^2}$ as discussed in Appendix B) are complementary to that in total intensity I, since the variation of the power baseline is not supposed to be polarized. We also corrected for the rotation of the linear feeds in parallactic angle, which otherwise would cause sinusoidal variations in the Q and U components. The Faraday rotation across the band, if adopting the rotation measure of PSR J1745−2900, is calculated to be approximately 4°.2. This suggests that the existence of rotation measure is likely to only have a minimal impact on the search sensitivity in Q and U (though other pulsars in the neighborhood may well have quite different RMs than the magnetar). The detection significance (signal-to-noise ratio; S/N) of the Fourier power for a pulsar candidate was calculated by summing a number of 16 Fourier harmonics. For each candidate with S/N > 2, we folded the total intensity time series with respect to its characteristics (period, period derivative, and jerk) and visually inspected the constructed signal.

Table 1 summarizes the number of candidates with S/N > 2 from the search. It can be seen that overall the segmented search produces significantly more candidates, mainly due to the additional parameter space explored. The searches in Stokes Q, U, and V yield substantially fewer candidates, reflecting the smaller contamination of their (zero-mean) time series by baseline variations. The GC magnetar J1745−2900 was blindly detected in all searches conducted in the 2017 campaign, except for the segmented searches in V due to a sensitivity limit. Figure 3 shows the detection of J1745−2900 in all four Stokes parameters from the searches using the full length of the observation. The S/Ns are in turn 28, 33, 22, and 4 for I, Q, U, and V, which demonstrates the success of finding pulsars with polarization components. The GC magnetar was not found in the blind search from the 2018 campaign, largely due to the fact that it was not covered by the synthesized beam of ALMA during the observation as illustrated in Figure 1. Folding the data with a pulsar ephemeris obtained from low-frequency monitoring observations (Desvignes et al. in prep.) revealed a weak and time-varying detection, indicating that its signal was collected in the side lobe of the array, which rotated with respect to the sky along the phase center during the tracking. The average strength of the signal is roughly an order of magnitude lower than that from the 2017 observation, so a nondetection from the blind search is expected as it falls under the search sensitivity as will be discussed in Section 4.1. Apart from the GC magnetar, no other evident pulsar candidate has been found.

3.2. Single-pulse Search

In addition to periodic signals, we have also searched for single bright pulses from pulsars or from transient sources such as those that emit fast radio bursts. Note that for searches at decimeter wavelengths, the dispersion sweep and multibeam comparisons are crucially useful criteria for distinguishing terrestrial signals from possible astrophysical events (e.g., Burke-Spolaor et al. 2011); however, these tools are not available with our millimeter observations. In light of such constraints, we developed a search scheme using the polarization property as the main criterion. As seen in previous observations, bright individual pulses commonly exhibit significant polarization at decimeter wavelengths (Lorimer & Kramer 2005; Petroff et al. 2016). This has also been indicated in a few pulsars at 3 mm wavelength (Torne et al. 2017; Liu et al. 2019). Thus, the coincidence of detection in both total intensity and one (or more) of the other polarization components can be applied during the candidate selection to find actual astronomical signals, assuming that terrestrial signals caught during the observations were not significantly polarized. Therefore, we carried out a single-pulse search to the time series in total intensity I, linear L, and circular V polarization, with the SINGLE_PULSE_SEARCH.PY program in PRESTO. Since the intrinsic V component of a pulsar can be of either a positive or negative sign, for the search in V we first subtracted the mean of the time series and carried out an additional search to the data multiplied by −1. Then we checked the time of event for all candidates above 7σ significance and kept those which were detected simultaneously in I and either L or V. In total, we have detected three events (all from I and L component) from the 2017 campaign and none from 2018. All event times coincide with the phase of the pulse profile of PSR J1745−2900, suggesting that these events are very likely to be individual pulses of the GC magnetar (see Section 3.3).

3.3. The Magnetar Signal

The 2017 observations offer a great opportunity to study the emission property of the GC magnetar, in particular its polarization. Figure 4 shows the polarization profile of the magnetar, together with its linear polarization position angle (Ψ) swing and the three individual pulses detected from the single-pulse search described in Section 3.2. It can be seen that the magnetar pulse profile is nearly 100% linearly polarized and the circular polarization component is also clearly seen. The high degree of linear polarization was already indicated by previous observations with the IRAM 30 m telescope at 3 mm wavelength (Torne et al. 2017). To study the emission geometry of the GC magnetar, we fitted the rotating-vector model (RVM) to the obtained position angle (Ψ) swing as described in Radhakrishnan & Cooke (1969)[22]:

$$\tan(\Psi_0 - \Psi) = \frac{\sin\alpha\sin(\phi - \phi_0)}{\sin(\alpha+\beta)\cos\alpha - \cos(\alpha+\beta)\sin\alpha\cos(\phi-\phi_0)}, \quad (2)$$

[22] Here we use the usual IAU convention where measured position angle increases counterclockwise on the sky, as discussed in Everett & Weisberg (2001)

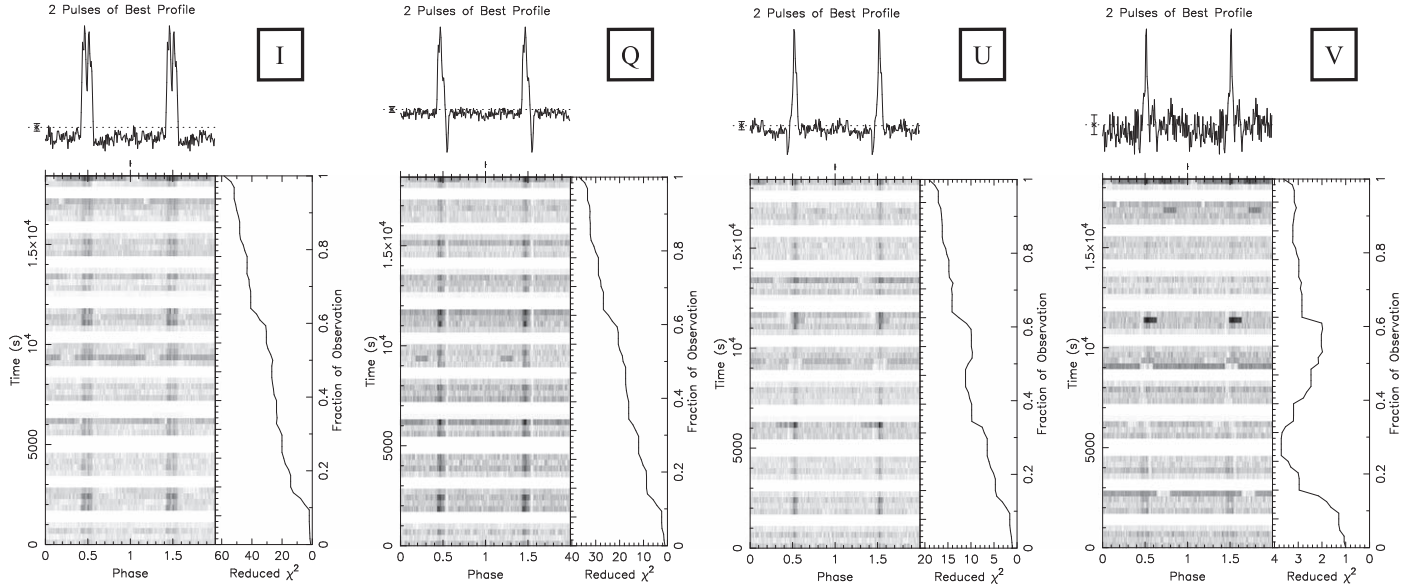

Figure 3. Detection of the GC magnetar PSR J1745−2900 from the blind search with the full length of the 2017 campaign using the four Stokes parameters. In all of the four cases, the magnetar was found as the candidate with the highest detection significance from the search.

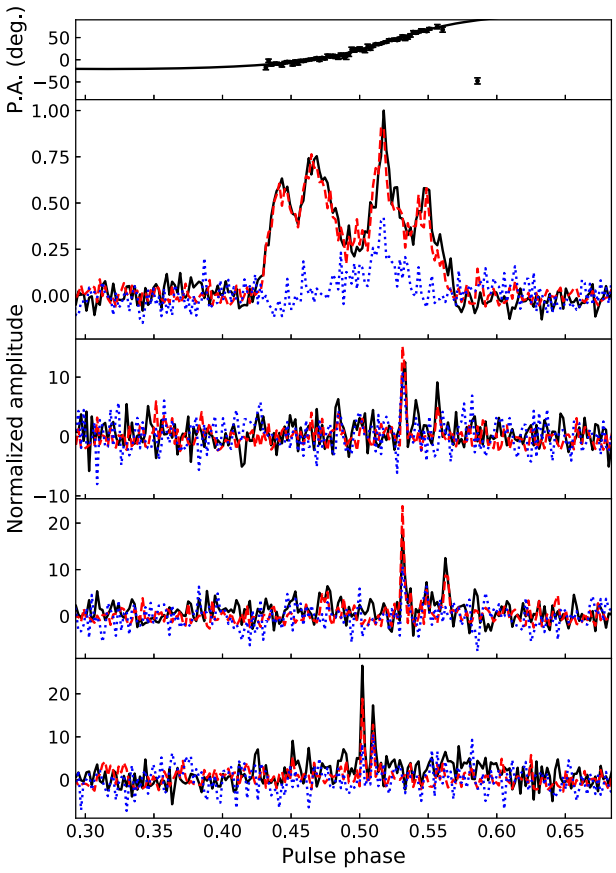

Figure 4. Polarimetric signals of the GC magnetar from the 2017 campaign. The top two panels are the polarization position angles and the polarization average profile, respectively. The profile is an average of approximately 2000 rotations. The bottom three panels are the three single pulses blindly detected in our search as discussed in Section 3.2. The solid line in the top panel stands for the RVM fit to the position angles. The solid black, dashed red, and dotted blue lines in the rest of the panels represent total intensity, linear, and circular component, respectively. The intensities are normalized with respect to the peak of the average profile in the second panel from the top.

where ϕ is the pulse phase, α is the magnetic inclination angle, and β is the impact parameter (angle between the magnetic axis and line of sight). The best-estimated values are: $\alpha = 110^{+16}_{-18}$ deg, $\beta = -20.0^{+3.0}_{-1.7}$ deg (1σ confidence interval). We also derived the mean flux density of the GC magnetar to be 0.39 ± 0.01 mJy based on the radiometer equation (detailed in Section 4.1), up to an order of magnitude weaker than previously reported at 3 mm wavelength (Torne et al. 2015, 2017). This is however in general consistent with measurements from some of the monitoring campaign with IRAM 30 m telescope (Torne et al. 2021).

From Figure 4, it can be seen that the three single pulses have peak intensities approximately 10–30 times of the average over all pulses. They individually show a high fraction in linear polarization as is also observed in the integrated profile. The single pulses occur at phases corresponding to the trailing part of the integrated profile. The subpulse structure is seen in all three cases, as also reported from previous single-pulse studies of the GC magnetar at lower frequencies (Pearlman et al. 2018; Wharton et al. 2019).

4. Survey Sensitivity

4.1. Limitation by Noise

For a given pulsar survey, its sensitivity can be theoretically derived with the radiometer equation. With a requested S/N of detection, the minimum detectable mean flux density of the pulsar can be approximated by Lorimer & Kramer (2005)[23]:

$$S_{\rm min} = \frac{({\rm S/N}){\rm T_{sys}}}{G\sqrt{n_{\rm p} t_{\rm int} \Delta\nu}} \sqrt{\frac{W}{P - W}}, \quad (3)$$

where $T_{\rm sys}$ is the system temperature, G is the telescope gain, n_p is the number of polarizations, $t_{\rm int}$ is the integration time, $\Delta\nu$ is

[23] Note that this formula is a valid approximation only when $P \gg W$. See Cordes & Chernoff (e.g., 1997) and Lazarus et al. (e.g., 2015) for extended discussions on this topic and more generic expressions.

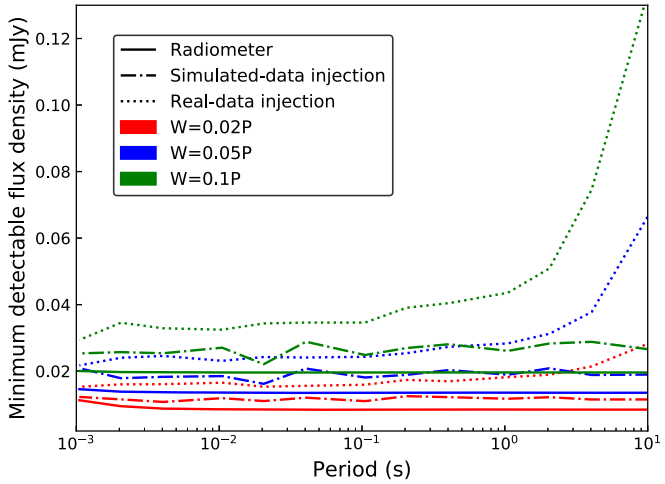

Figure 5. Minimum detectable flux density (with a 7σ detection threshold) of the GMVA survey as a function of the pulsar period, estimated with the radiometer equation, injection into simulated data, and injection into the real data. Limits are shown for three typical values of pulse width (W). The pulse width of PSR J1745−2900 is approximately 0.1 P from the GMVA 2017 observation.

the bandwidth, P is the pulsar rotational period, and W is the effective pulse width. For our observation at Band-3, we use $G = 1.15$ K Jy^{-1} and $T_{\rm sys} = 51$ K as a result from the QA2 analysis which also takes into account the phasing efficiency of the array (Goddi et al. 2019). However, sensitivity estimates using the formula above would have a few caveats when applying to our data. First, it is known to overestimate the sensitivity for slow pulsars (e.g., $P > 1$ s) due to the presence of red noise in the data (Lazarus et al. 2015). Second, the data are effectively not evenly sampled as a consequence of the gaps between individual scans. In addition, there could be impact on the sensitivity by other (periodic) signals or non-Gaussianity in the data. Thus, similar to Lazarus et al. (2015), we estimated the sensitivity of our search using a few different schemes described as follows. First, we directly calculated the values with the radiometer equation. Second, we simulated a fake pulsar signal along with white-noise data of the same length, spacing, and rms as the real observations, and carried out a real search with our pipeline. Furthermore, we directly injected a fake pulsar signal into the real data and performed a search with our pipeline.

Figure 5 summarizes the sensitivity estimates described above. It can be seen that the estimates from radiometer equation and from injection into simulated data lead to consistent minimum detectable flux densities, while values from the latter are approximately 20% higher possibly due to the existence of gaps in between individual scans. Injection into real data resulted in slightly higher limits for fast spinning pulsars, which is around 0.03 mJy, and became up to a factor of 5 higher for slow pulsars ($P \gtrsim 1$ s) with wide pulse width. This is expected due to the presence of red noise and other terrestrial signals in the real data.

4.2. Sensitivity to Binary Motion

The observed period of a pulsar can change significantly during the observation as a result of the Doppler effect if it is in orbital motion and thus accelerated. The variation depends on the orbital phase at the epoch of observation and is approximately linear in time if the pulsar endures roughly a constant line-of-sight acceleration ($a_{\rm l}$) during the observation (Ransom et al. 2002). However, if the observing length ($T_{\rm obs}$) is a significant fraction of orbital period (e.g., $T_{\rm obs} \gtrsim 10\%\ P_{\rm b}$), the derivative of the acceleration, commonly referred to as jerk ($j_{\rm l}$), is then required to better describe the variation of pulsar period (Ransom et al. 2002; Bagchi et al. 2013; Eatough et al. 2013a; Liu et al. 2014; Andersen & Ransom 2018). While acceleration and jerk searches have been widely studied in searches for binary pulsars with solar-mass companions, important differences when searching for pulsars in orbit with Sgr A* have only been pointed out very recently by Eatough et al. (2021, in preparation). Here, it was shown that in deep searches for millisecond pulsars (MSPs) in long-period circular orbits around Sgr A* $P_{\rm b} \sim 2$ yr, even the constant acceleration is enough to make z exceed the current maximum value configurable in PRESTO ACCELSEARCH — thereby placing lower limits on the minimum Sgr A* orbital period detectable for a pulsar of a given spin period.

Following, e.g., Bagchi et al. (2013), the line-of-sight acceleration and jerk of an orbital pulsar can be written as:

$$a_{\rm l} = -\left(\frac{2\pi}{P_{\rm b}}\right)^2 \frac{a_{\rm p} \sin i}{(1-e^2)^2} \sin(A_{\rm T} + \omega)(1 + e\cos A_{\rm T})^2\,, \quad (4)$$

and

$$j_{\rm l} = -\left(\frac{2\pi}{P_{\rm b}}\right)^3 \frac{a_{\rm p} \sin i}{(1-e^2)^{7/2}}(1 + e\cos A_{\rm T})^3 \cdot [\cos(A_{\rm T} + \omega) + e\cos\omega - 3e\sin(A_{\rm T} + \omega)\sin A_{\rm T}], \quad (5)$$

where $a_{\rm p}$, e, i, and A_T are the semimajor axis, eccentricity, inclination, and true anomaly of the pulsar orbit. In the Fourier domain, $a_{\rm l}$ and $j_{\rm l}$ correspond to shifts in the Fourier frequency bin (z) and its derivative (w) within an entire observation of length $T_{\rm obs}$ as (Andersen & Ransom 2018)

$$z = \frac{a_{\rm l} h f T_{\rm obs}^2}{c}, \quad (6)$$

and

$$w = \frac{j_{\rm l} h f T_{\rm obs}^3}{c}, \quad (7)$$

where c, f, h are the speed of light, fundamental frequency of the pulsar rotation, and the index of the Fourier harmonic being considered. In practice, the Fourier-domain search is blindly performed, covering a range of possible z and w values, respectively. Each range is symmetric around zero and given a half width that covers the largest possible absolute z or w from an entire orbit. While in reality the absolute z and w reach their maximum at different orbital phase, e.g., observing epochs, a blind search needs to cover both maxima at the same time so as to ensure an optimal survey sensitivity at any potential orbital phase. With the equations above, the ratio of the maximum of absolute z and w out of an entire orbit can be written as

$$\frac{\max(|w|)}{\max(|z|)} = \frac{T_{\rm obs}}{P_{\rm b}(1-e^2)^{3/2}} f(e, \omega), \quad (8)$$

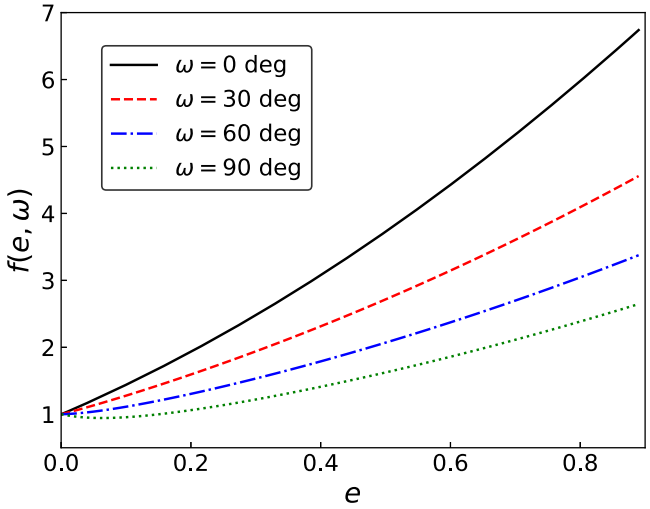

Figure 6. Value of $f(e, \omega)$ in Equation (8) as a function of e for a few options of ω. In general, $f(e, \omega)$ is increased from unity when the orbit becomes more eccentric, while having a local minimum of approximately 0.94 at $e \sim 0.1$ when ω is close to 90 deg. A given e, $f(e, \omega)$ is at maximum when $\omega = 0$ or 180 deg. The value range of $f(e, \omega)$ is identical when $\omega \in [0, 90)$, [90, 180), [180, 270), and [270, 360) deg, respectively.

where $f(e, \omega) = 1$ for $e = 0$ and in general increases for a larger e as shown in Figure 6. It can be seen that the relative value of $\max(|w|)$ to $\max(|z|)$ becomes larger for more compact and eccentric orbits, and longer observations. This shows the increasing importance of including a jerk search under these circumstances.

Accordingly, for a given observation we can calculate the maximum absolute z and w values from a range of orbits to see if the search is in practice sensitive to pulsars in those orbits. Here for the estimate of our search, we mainly consider two scenarios: (1) a pulsar in orbit with Sgr A*; (2) a pulsar in a close binary with a degenerate companion (a neutron star or white dwarf). We also consider the impact on the detectability by orbital eccentricity where jerk effects (covered by the w term) become more significant in comparison with the analysis presented in Eatough et al. (2021, in preparation). The results for our survey concerning the first scenario are presented in Figure 7. It can be seen that for an ordinary pulsar ($P = 100$ ms), a maximum $|z|$ value of 1200 is sensitive to orbital periods down to $\sim$0.5 yr for a moderate eccentricity ($e \sim 0.5$) and further down to 0.2 yr if the eccentricity is low ($e \sim 0.1$). For an MSP, these are restricted to $\sim$5 yr and 2 yr, respectively. The searches that use $1/3$ of the entire observation and the same maximum $|z|$, significantly improves the coverage of the orbital parameters space. For an ordinary pulsar, it is expected to be sensitive to the vast majority of the possible orbits except for those of a very short orbital period and high eccentricity. For an MSP, the segmented search begins to cover a significant fraction of possible orbits with $P_b < 1$ yr. Exploration in the space of jerk in this scenario is much less required except only for short and highly eccentric orbits, as indicated from the scaling law by Equation (8). For a choice of $\max(|z|) = 1200$, a corresponding $\max(|w|) = 40$ used in our search is just enough to cover the same range of orbits while using the full length of the observation. For the segmented searches that use $1/3$ of the full length, the required $\max(|w|)$ is approximately 400 which is well below 1500, which we used. Our results are in broad consistency with what have been reported by Eatough et al. (2021 in preparation; shown in Figure 7), when the orbital eccentricity is low ($e = 0.1$).

For many of the known binary pulsars, our 5.2 hr long data set is comparable to or larger than the orbital period (Manchester et al. 2005). Thus, the segmented search is necessary to provide sensitivity for a significant population of binary pulsars, in particular those with $P_b \lesssim 1$ d. Figure 8 shows the maximum z and w values required in the segmented search for a range of orbital period and eccentricity. Here two common types of binary pulsars are considered: a mildly recycled pulsar with a neutron star companion ($1.4\,M_\odot$) and an MSP with a white dwarf companion ($0.5\,M_\odot$) (Lorimer & Kramer 2005). It can be seen that with maximum z of 1200 and maximum w of 1500 used in our search, the coverage of orbit is approximately down to 0.7 d in the former and 2 d in the latter case, for a moderate orbital eccentricity ($e \sim 0.5$). These constraints drop to 0.5 d and 1 d, respectively, if the eccentricity is assumed to be low ($e \sim 0.1$).

The aforementioned sensitivity limit of our search on potential pulsar orbits should be considered as constraints on the "worst-case scenario," since it requires the survey to be conducted with an "optimal" sensitivity. In practice, a pulsar in a tight orbit, where a jerk search or a higher order derivative of acceleration is needed to approximate the orbital motion, could still be detected if its signal is sufficiently strong after the systematic reduction. In the Fourier domain, the amplitudes of high-order harmonics of the pulsar rotational frequency are reduced, which causes harmonic summing to also produce a smaller detection statistic. It is also possible that the pulsar happens to be observed at a favorable orbital phase, where the instantaneous values of z and w are below the limits, while their maxima over an entire orbit are not. Lastly, single pulses are unaffected by imperfect removal of the orbit from arrival times.

5. Discussion

It is anticipated that the GC hosts a substantial population of pulsars in its inner parsec with the most optimistic estimate of up to $\sim$100 pulsars[24] with $P_b \lesssim 10$ yr that can be covered by our search (e.g., Pfahl & Loeb 2004; Wharton et al. 2012; Chennamangalam & Lorimer 2014). However, as discussed in Eatough et al. (2015) and Liu & Eatough (2017), most surveys by now are, in practice, very limited in exploring the GC pulsar population. To examine how deeply our survey can probe the GC pulsars, we have calculated the luminosity threshold at 87 GHz based on the estimated survey sensitivity in Section 4. As a comparison, we also estimated the anticipated sensitivity of a Q-band survey with the ALMA, once its Band 1 is fully operational. For this we applied a similar observing setup (6 hr tracking and effective on-source time approximately 50%) to the GMVA campaign, 8 GHz bandwidth (with all four spectral windows), the same telescope gain as in Band 3, a system temperature of 50 K and a central frequency of 42 GHz (Huang et al. 2016). For a given pulsar period, the system sensitivity was then derived based on the estimate in Figure 5 with the radiometer equation and translated into a luminosity threshold at 87 GHz assuming a spectral index of -1.6.

These limits were compared with the anticipated luminosities of a large pulsar population. To select the samples of pulsars,

[24] This is merely a population estimate and does not take into account the beaming fraction of pulsars, roughly 20% estimated from previous observations (e.g., Lorimer & Kramer 2005).

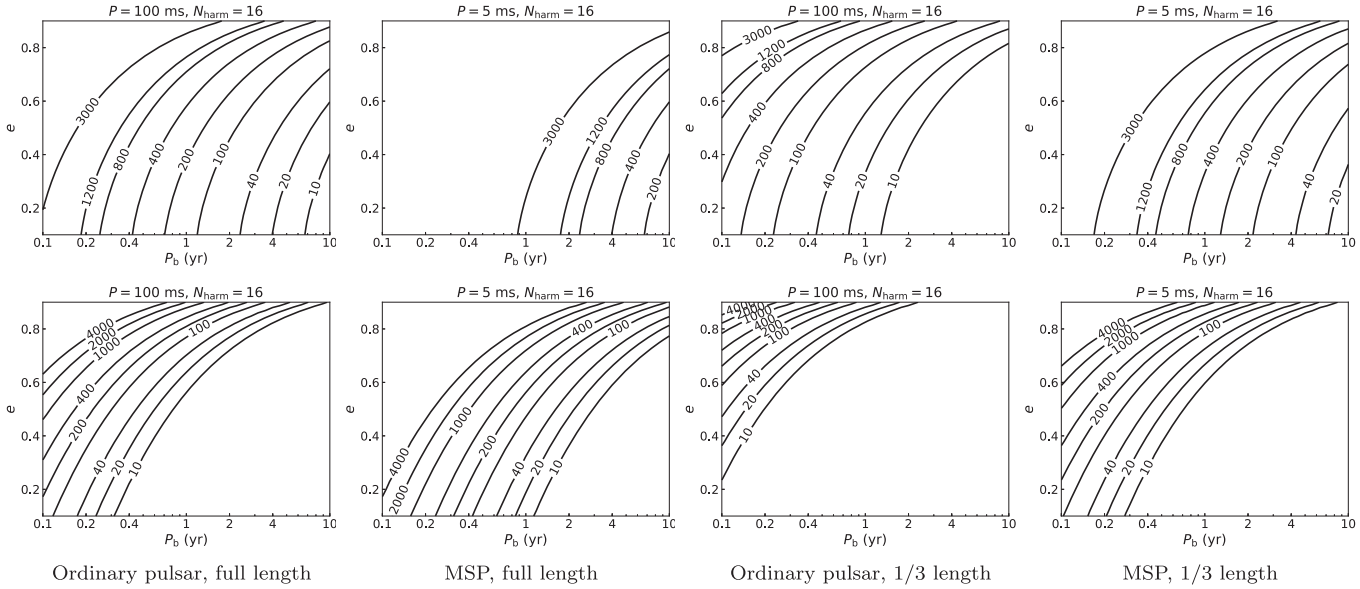

Figure 7. zmax (upper row) and wmax (lower row) values required in PRESTO for our searches to retain optimal sensitivity to pulsars in orbit with Sgr A* for a range of orbital periods and eccentricities. Here we use the length of the 2017 campaign (5.1 hr in total) and the 2018 campaign has a similar length. As mentioned in Section 3.1, the zmax, wmax values used in our searches are 1200, 40 for the full data length, and 1200, 1500 for the 1/3 data length, respectively.

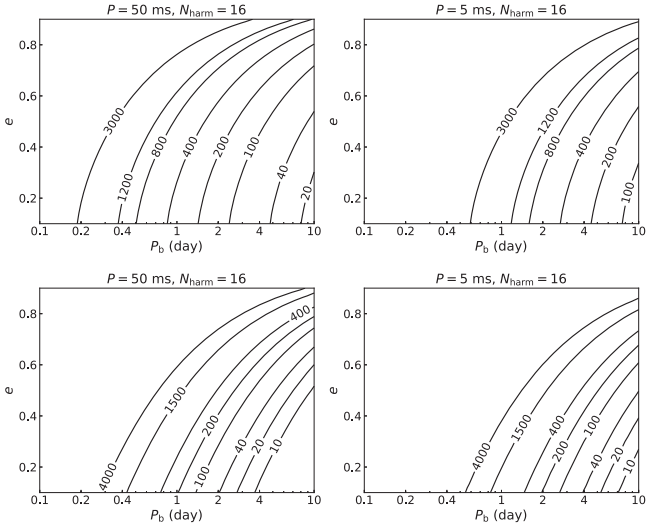

Figure 8. Maximum of z (upper row) and w (lower row) values required in our segmented search (1/3 length) for orbits of different periods and eccentricities in a binary pulsar system. The companion is assumed to be a 1.4 $M_\odot$ neutron star for the case of a mildly recycled pulsar ($P = 50$ ms) and a 0.5 $M_\odot$ white dwarf for the case of a MSP ($P = 5$ ms). The full observing length used here is the same as in Figure 7. For reference, the zmax, wmax values used in the 1/3-length searches are 1200 and 1500, respectively, as mentioned in Section 3.1.

we used the ATNF pulsar catalog (Manchester et al. 2005) and chose all pulsars with flux density measurements around 1.4 GHz or above because the pulsar spectrum at lower frequencies tends to deviate from a simple power law (e.g., Kijak et al. 2011; Jankowski et al. 2018). This kept 70% (1932 out of 2796) of the overall pulsar population for the analysis thereafter. Then for pulsars with a reported spectral index, we extrapolated the flux density to 87 GHz assuming the power-law spectrum extends up to that frequency. If no measurement of spectral index is available, we applied a random value drawn from a normal distribution (with mean of −1.6 and standard deviation of 0.54), reported in Jankowski et al. (2018), which was obtained based on the statistics of ∼300 pulsars. Exceptions are PSR J0835−4510 (the Vela pulsar), PSR B0355+54, Swift J1818.0−1607, PSR J1745−2900, and XTE J1810−197, for which we simply used the reported flux density measurements at 87 GHz (Morris et al. 1997; Liu et al. 2019; Torne et al. 2020a, 2020b, and this work). The distance measurements are mostly based on the DM and the YMW16 Galactic free-electron density model (Yao et al. 2017), except for the Vela pulsar, PSR B0355+54, and XTE J1810−197, where a parallax distance was used (Caraveo et al. 2001; Chatterjee et al. 2004; Ding et al. 2020), and PSR J1745−2900 for which we applied the distance to the GC reported by Gravity Collaboration et al. (2021). We repeated the aforementioned procedure for 1000 realizations to accumulate a robust assessment of the pulsar population detectable by the surveys. Figure 9 presents the results from one typical iteration.

It has been found that our ALMA-GMVA survey is able to detect only the most luminous pulsars, approximately the top 4% (average from all realizations) of all selected pulsars. Meanwhile, the survey would already be sensitive enough to detect all three radio-loud magnetars (Swift J1818.0−1607, PSR J1745−2900 and XTE J1810−197), which have been detected at millimeter wavelength[25], if they were located in the GC. The ALMA Q-band survey has the potential to increase the fraction to approximately 14%, nearly a factor of 4 improvement. A similar investigation on probing the GC pulsar population with ALMA was recently reported in Torne et al. (2021), where a result in line with that presented here can be found. Note that, as shown in Figure 9, the surveys are very unlikely to be sensitive to any MSPs in the GC.

The estimate above largely depends on extrapolation of pulsar spectra from decimeter and centimeter to 3 mm wavelength with a simple power-law model. This assumption has a significant number of exceptions where a more complex model, such as a broken power law, needs to be introduced to

[25] The pulse widths of Swift J1818.0−1607 and XTE J1810−197 reported in Torne et al. (2020a) and Torne et al. (2020b), respectively, are both close to 0.05 P used in the sensitivity curve plotted in Figure 9.

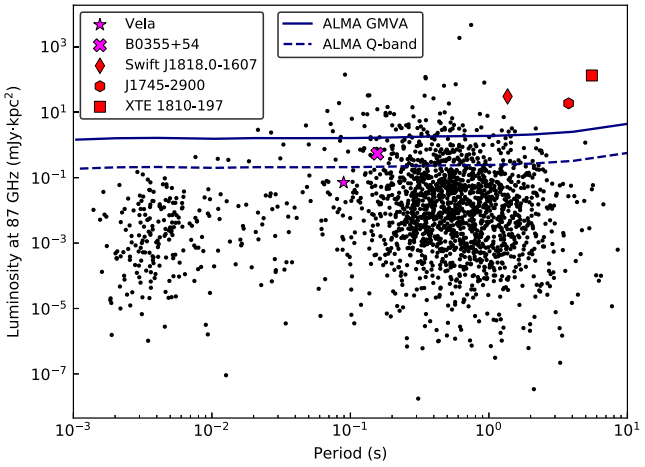

Figure 9. Sensitivity of ALMA GC surveys with respect to the 87 GHz luminosity of a large pulsar population. The black dots represent luminosities calculated from one typical iteration out of a thousand in each of which a random spectral index was drawn from a normal distribution for pulsars without a reported spectral index measurement. The ALMA-GMVA sensitivity curve is obtained from the injection into real data with $W = 0.05$ P, shown in Figure 5. Five pulsars that have been detected at a millimeter wavelength are highlighted, where the purple and red color represent ordinary pulsar and magnetar, respectively.

fit the observed pulsar spectrum (Maron et al. 2000; Kijak et al. 2011; Jankowski et al. 2018). So far, only a few dozens of pulsars have had their emission properties studied above 10 GHz (Wielebinski et al. 1972; Bartel et al. 1977; Sieber & Wielebinski 1987; Wielebinski et al. 1993; Kramer et al. 1996, 1997; Löhmer et al. 2008; Keith et al. 2011; Hankins et al. 2016; Torne et al. 2017; Liu et al. 2019), so that an average spectral index calculated from those sources may be biased toward flatter values. On the other hand, some individual pulse components have markedly different spectra, leading to possibly complex pulsar spectra overall and rather different pulse profiles at high frequencies (see e.g., PSR B0144+59, Löhmer et al. 2008). There are also indications that the spectrum could turn up at millimeter wavelengths (Kramer et al. 1997). This is not completely unexpected (Cordes 1979; Kramer et al. 1997) as some theories predict the existence of other spectral components rising somewhere in between the radio and infrared bands, e.g., due to incoherent curvature emission (Michel 1982) or inverse Compton scattering of low-frequency radio photons (Blandford & Scharlemann 1976; Lyutikov 2013). Therefore, additional sample studies are in great demand to fully understand pulsar emissions and the potential of pulsar surveys in the mm-wavelength regime.

6. Conclusions

We have carried out the first GC pulsar and transient search with ALMA, using data collected in the GMVA 2017 and 2018 campaigns. Periodicity searches were conducted on time series of all four Stokes parameters, with acceleration and jerk, and in both the full length and 1/3 length of the entire observation. Single-pulse searches were performed on time series in total intensity, linear, and circular polarization. We obtained the first polarization profile of the GC magnetar at a millimeter wavelength and found that it is close to 100% linearly polarized. While no new pulsar is found, we estimated the survey sensitivity using both the radiometer equation and a signal-injection scheme, and evaluated its capability of finding pulsars with orbital motion. Finally, we showed the survey is only sensitive to the most luminous pulsars in the overall population and a survey using ALMA Band 1 has the potential to probe much deeper into the GC pulsar population. Future searches at a millimeter wavelength is necessary also to increase the detection probability of magnetars and many other pulsars of a transient nature and pulsars at different phases of eccentric orbits.

We thank Eduardo Ros and Marylin Cruces for carefully reading the manuscript and providing valuable suggestions. K.L., G.D., R.P.E., R.K., M.K., P.T., R.W., C.G., F.A., C.D.B., H.F., A.N., L.R., and L.S. acknowledge the financial support by the European Research Council for the ERC Synergy grant Black-HoleCam under contract no. 610058. RPE is supported by a "FAST Fellowship" under the "Cultivation Project for FAST Scientific Payoff and Research Achievement of the Center for Astonomical Mega-Science, Chinese Academy of Sciences (CAMS-CAS)." J.M.C. and S.C. acknowledge support from the National Science Foundation (NSF AAG-1815242). S.M.R. is a CIFAR Fellow. R.S.L is supported by the Max Planck Partner Group of the MPG and the CAS and acknowledges support from the Key Program of the National Natural Science Foundation of China (grant No. 11933007) and the Research Program of Fundamental and Frontier Sciences, CAS (grant No. ZDBS-LY-SLH011). L.S. was supported by the National SKA Program of China (2020SKA0120300), the National Natural Science Foundation of China (11991053, 11975027), the Young Elite Scientists Sponsorship Program by the China Association for Science and Technology (2018QNRC001), and the Max Planck Partner Group Program funded by the Max Planck Society. The ALMA Phasing Project was principally supported by a Major Research Instrumentation award from the National Science Foundation (award 1126433) and an ALMA North American Development Augmentation award to Cornell University. The ALMA Pulsar Mode Project was supported by an ALMA North American Study award.

This research has made use of data obtained with the Global Millimeter VLBI Array (GMVA), which consists of telescopes operated by the MPIfR, IRAM, Onsala, Metsahovi, Yebes, the Korean VLBI Network, the Greenland Telescope, the Green Bank Observatory, and the Very Long Baseline Array (VLBA). The National Radio Astronomy Observatory is a facility of the National Science Foundation operated under cooperative agreement by Associated Universities, Inc. The VLBA is a facility of the National Science Foundation operated under cooperative agreement by Associated Universities, Inc. The data were correlated at the correlator of the MPIfR in Bonn, Germany.

Facilities: ALMA, GMVA.

Software: PRESTO.

Appendix A
Systematics and Cleaning Scheme

The raw baseband voltage data collected during the GMVA observations were converted into intensity time series as part of the data processing offline. Figure 10 (upper panel) shows the time series from one of the scans as an example. A cyclic power drop-off feature is immediately noticeable on top of the overall baseline and was found to be of the same period as the phasing cycle of the APP which is 18.192 s. Figure 11 shows the feature averaged with respect to its period over the entire

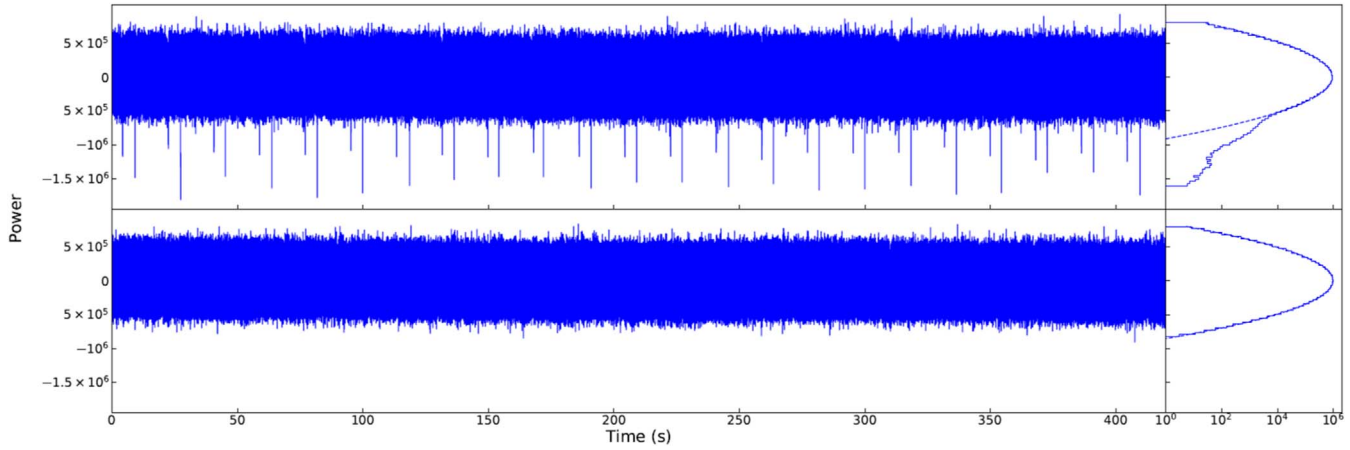

Figure 10. Timeseries from one 7 min scan on Sgr A* with the mean power subtracted. The upper panel shows the original data where power drop offs are seen to occur repetitively every 18.192 s. A histogram of the time samples exhibits a clear deviation at the negative end from a best-fitted Guassian function. The lower panel shows the same chunk of data after application of the cleaning scheme, where the statistics of the time samples are well fitted with a Gaussian distribution.

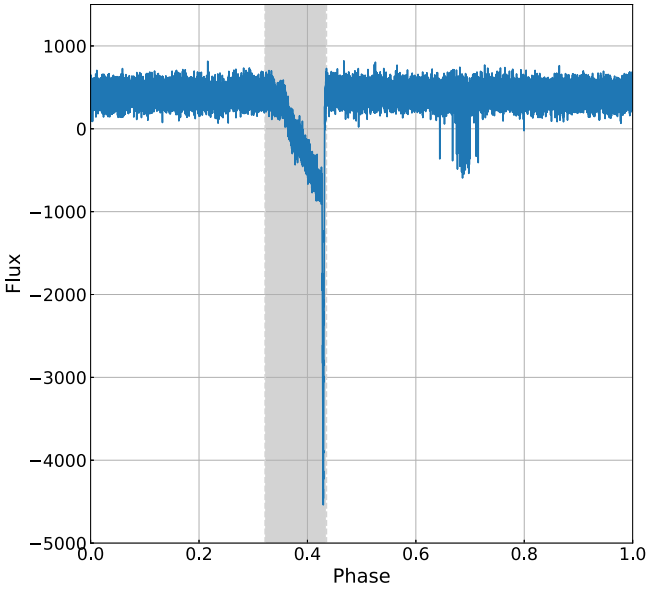

Figure 11. Averaged profile of the time series in Figure 10 with respect to the period of phasing cycle in APP. The power drop off around phase 0.4 coincides with the dump time in between two subscans and its phase range is marked in gray color. The drop offs around phase 0.7 are associated with the injection of a new phasing solution into the system.

time span in Figure 10. It can be seen that in every cycle, the occurrence of power drop-off clusters within two phase ranges (around 0.4 and 0.7), which in turn have been corresponded to a 2.064 s "dump time" in between 16.128 s observing subscans and the refresh of the phasing solution, respectively (detailed in Goddi et al. 2019). A zoomed browse through the time series has found that during the dump time, the baseline drops progressively in different numbers of steps for each cycle but always recovers within a short time window in the end. This is also indicated by the steep edge at the trailing side of the averaged feature in Figure 11. Thus, the trailing edge can be used as the reference to identify the phase range of the dump time (shown as the filled region in Figure 11), which was not known beforehand. The power drop offs associated with injection of a new phasing solution are in general 2–4 s trailing the dump time but not precisely periodic since the computing time cost to obtain the solution is different in every cycle. Nonetheless, the drop off usually exhibits as a simple negative step function without significantly altering the level of baseline afterwards.

Accordingly, we have established a dedicated scheme to mitigate those systematics in the data. For every scan, we first folded the time series with respect to the phasing period and used the averaged feature from dump time to determine its absolute phase. Then we returned to the time series and replaced the samples during the dump time with random noise created using mean and rms obtained from the subscan right before. The power drop-off caused by the refresh of phase solution can be effectively cleaned with the built-in clip function in PRESTO's `prepdata` program while creating the time series. An example of the cleaned data after applying the scheme can be found in the lower panel of Figure 10. It is clearly seen that the vast majority of the systematics has been removed and the distribution of time samples is well modeled by a Gaussian function.

Appendix B
Baseline Variation in Stokes

Here we investigate the property of polarization components when the input signal of a data-recording system has a time variability as a consequence of, e.g., fluctuation in system temperature. For simplicity, we consider an ideal orthogonal system where the two linear feeds are equally illuminated by the input signal. The signals from the two polarization channels can be expressed as:

$$\begin{cases} x = \hat{a}_{\rm x} + \hat{b}_{\rm x}\boldsymbol{i} \\ y = \hat{a}_{\rm y} + \hat{b}_{\rm y}\boldsymbol{i}, \end{cases} \tag{B1}$$

where $\hat{a}_{\rm x}$, $\hat{b}_{\rm x}$, $\hat{a}_{\rm y}$, $\hat{b}_{\rm y}$ are all independent variables. Assuming that the input signal is pure Gaussian noise with time-dependent variance, we have:

$$\begin{cases} \overline{\hat{a}_{\rm x}} = \overline{\hat{b}_{\rm x}} = \overline{\hat{a}_{\rm y}} = \overline{\hat{b}_{\rm y}} = 0, \\ \overline{\hat{a}_{\rm x}^2} = \overline{\hat{b}_{\rm x}^2} = \overline{\hat{a}_{\rm y}^2} = \overline{\hat{b}_{\rm y}^2} = \sigma^2(t), \end{cases} \tag{B2}$$

where $\sigma^2(t)$ is the actual detected power as a function of time. Accordingly, the four Stokes parameters are written as:

$$\begin{cases} \bar{I} = \bar{xx^*} + \bar{yy^*} = 4\sigma^2(t) \\ \bar{Q} = \bar{xx^*} - \bar{yy^*} = 0 \\ \bar{U} = 2\bar{\Re(x^*y)} = 2\bar{\hat{a}_x\hat{a}_y} + 2\bar{\hat{b}_x\hat{b}_y} = 0 \\ \bar{V} = 2\bar{\Im(x^*y)} = 2\bar{\hat{a}_x\hat{b}_y} + 2\bar{\hat{a}_y\hat{b}_x} = 0. \end{cases} \tag{B3}$$

Thus, while the power in I changes as a function of time, there is no resulting time variability in the other Stokes parameters, Q, U, and V, as far as the input signal is unpolarized. Meanwhile, the detection in linear polarization L, is written as:

$$\bar{L} = \sqrt{\bar{L}^2} = \sqrt{\overline{Q^2 + U^2}} = 4\sigma^2(t), \tag{B4}$$

where

$$\overline{Q^2} = \overline{(xx^* - yy^*)^2} = \overline{\hat{a}_x^4} + \overline{\hat{b}_x^4} + \overline{\hat{a}_y^4} + \overline{\hat{b}_y^4} = 8\sigma^4(t), \tag{B5}$$

$$\overline{U^2} = \overline{[2\Re(x^*y)]^2} = \overline{\hat{a}_x^2\hat{a}_y^2} + \overline{\hat{b}_x^2\hat{b}_y^2} = 8\sigma^4(t). \tag{B6}$$

Therefore, the detection of linear polarization will also be affected when the power in I exhibits a time variability.

ORCID iDs

Kuo Liu https://orcid.org/0000-0002-2953-7376
Gregory Desvignes https://orcid.org/0000-0003-3922-4055
Ralph P. Eatough https://orcid.org/0000-0001-6196-4135
Ramesh Karuppusamy https://orcid.org/0000-0002-5307-2919
Michael Kramer https://orcid.org/0000-0002-4175-2271
Pablo Torne https://orcid.org/0000-0001-8700-6058
Robert Wharton https://orcid.org/0000-0002-7416-5209
Shami Chatterjee https://orcid.org/0000-0002-2878-1502
James M. Cordes https://orcid.org/0000-0002-4049-1882
Geoffrey B. Crew https://orcid.org/0000-0003-4056-9982
Ciriaco Goddi https://orcid.org/0000-0002-2542-7743
Scott M. Ransom https://orcid.org/0000-0001-5799-9714
Federico Abbate https://orcid.org/0000-0002-9791-7661
Geoffrey C. Bower https://orcid.org/0000-0003-4056-9982
Christiaan D. Brinkerink https://orcid.org/0000-0002-2322-0749
Heino Falcke https://orcid.org/0000-0002-2526-6724
Aristeidis Noutsos https://orcid.org/0000-0002-4151-3860
Antonio Hernández-Gómez https://orcid.org/0000-0001-7520-4305
Wu Jiang (江悟) https://orcid.org/0000-0001-7369-3539
Michael D. Johnson https://orcid.org/0000-0002-4120-3029
Ru-Sen Lu (路如森) https://orcid.org/0000-0002-7692-7967
Yurii Pidopryhora https://orcid.org/0000-0002-3523-9156
Luciano Rezzolla https://orcid.org/0000-0002-1330-7103
Lijing Shao https://orcid.org/0000-0002-1334-8853
Zhiqiang Shen (沈志强) https://orcid.org/0000-0003-3540-8746
Norbert Wex https://orcid.org/0000-0003-4058-2837

References

Andersen, B. C., & Ransom, S. M. 2018, ApJL, 863, L13
Aschenbach, B., Grosso, N., Porquet, D., & Predehl, P. 2004, A&A, 417, 71
Bagchi, M., Lorimer, D. R., & Wolfe, S. 2013, MNRAS, 432, 1303
Bartel, N., Sieber, W., & Wielebinski, R. 1977, A&A, 55, 319
Blandford, R. D., & Scharlemann, E. T. 1976, MNRAS, 174, 59
Boehle, A., Ghez, A. M., Schödel, R., et al. 2016, ApJ, 830, 17
Bower, G. C., Deller, A., Demorest, P., et al. 2014, ApJL, 780, L2
Bower, G. C., Deller, A., Demorest, P., et al. 2015, ApJ, 798, 120
Burke-Spolaor, S., Bailes, M., Ekers, R., Macquart, J.-P., & Crawford Fronefield, I. 2011, ApJ, 727, 18
Caraveo, P. A., De Luca, A., Mignani, R. P., & Bignami, G. F. 2001, ApJ, 561, 930
Chatterjee, S., Cordes, J. M., Vlemmings, W. H. T., et al. 2004, ApJ, 604, 339
Chennamangalam, J., & Lorimer, D. R. 2014, MNRAS, 440, L86
Cordes, J. M. 1979, SSRv, 24, 567
Cordes, J. M., & Chernoff, D. F. 1997, ApJ, 482, 971
Cordes, J. M., & Lazio, J. T. W. 1997, ApJ, 475, 557
De Laurentis, M., Younsi, Z., Porth, O., Mizuno, Y., & Rezzolla, L. 2018, PhRvD, 97, 104024
Deneva, J. S., Cordes, J. M., & Lazio, T. J. W. 2009, ApJL, 702, L177
Desvignes, G., Eatough, R. P., Pen, U. L., et al. 2018, ApJ, 852, L12
Dexter, J., Deller, A., Bower, G. C., et al. 2017, MNRAS, 471, 3563
Ding, H., Deller, A. T., Lower, M. E., et al. 2020, MNRAS, 498, 3736
Do, T., Hees, A., Ghez, A., et al. 2019, Sci, 365, 664
Doeleman, S. S., Weintroub, J., Rogers, A. E. E., et al. 2008, Natur, 455, 78
Eatough, R., Lazio, T. J. W., Casanellas, J., et al. 2015, in Proc. of Sci., Advancing Astrophysics with the Square Kilometre Array (Trieste: SISSA), 45
Eatough, R. P., Falcke, H., Karuppusamy, R., et al. 2013b, Natur, 501, 391
Eatough, R. P., Kramer, M., Lyne, A. G., & Keith, M. J. 2013a, MNRAS, 431, 292
Eckart, A., & Genzel, R. 1996, Natur, 383, 415
Eckart, A., Genzel, R., Hofmann, R., Sams, B. J., & Tacconi-Garman, L. E. 1993, ApJL, 407, L77
Eisenhauer, F., Genzel, R., Alexander, T., et al. 2005, ApJ, 628, 246
Event Horizon Telescope Collaboration, Akiyama, K., Alberdi, A., et al. 2019, ApJL, 875, L1
Everett, J. E., & Weisberg, J. M. 2001, ApJ, 553, 341
Falcke, H., Melia, F., & Agol, E. 2000, ApJL, 528, L13
Fish, V. L., Doeleman, S. S., Beaudoin, C., et al. 2011, ApJL, 727, L36
Genzel, R., Schödel, R., Ott, T., et al. 2003, Natur, 425, 934
Ghez, A. M., Becklin, E., Duchjne, G., et al. 2003, ANS, 527, 324
Ghez, A. M., Klein, B. L., Morris, M., & Becklin, E. E. 1998, ApJ, 509, 678
Gillessen, S., Plewa, P. M., Eisenhauer, F., et al. 2017, ApJ, 837, 30
Goddi, C., Falcke, H., Kramer, M., et al. 2017, IJMPD, 26, 1730001
Goddi, C., Martí-Vidal, I., Messias, H., et al. 2019, PASP, 131, 075003
Gravity Collaboration, Abuter, R., Amorim, A., et al. 2018, A&A, 618, L10
Gravity Collaboration, Abuter, R., Amorim, A., et al. 2020, A&A, 636, L5
Gravity Collaboration, Abuter, R., & Amorim, A. 2021, A&A, 647, A59
Hankins, T. H., Eilek, J. A., & Jones, G. 2016, ApJ, 833, 47
Huang, Y. D. T., Morata, O., Koch, P. M., et al. 2016, Proc. SPIE, 9911, 99111V
Issaoun, S., Johnson, M. D., Blackburn, L., et al. 2019, ApJ, 871, 30
Jankowski, F., van Straten, W., Keane, E. F., et al. 2018, MNRAS, 473, 4436
Johnson, M. D., Narayan, R., Psaltis, D., et al. 2018, ApJ, 865, 104
Johnston, H. M., & Kulkarni, S. R. 1991, ApJ, 368, 504
Johnston, S., Kramer, M., Lorimer, D. R., et al. 2006, MNRAS, 373, L6
Keith, M. J., Johnston, S., Levin, L., & Bailes, M. 2011, MNRAS, 416, 346
Kijak, J., Lewandowski, W., Maron, O., Gupta, Y., & Jessner, A. 2011, A&A, 531, A16
Kramer, M., Backer, D. C., Cordes, J. M., et al. 2004, NewAR, 48, 993
Kramer, M., Jessner, A., Doroshenko, O., & Wielebinski, R. 1997, ApJ, 489, 364
Kramer, M., Xilouris, K. M., Jessner, A., Wielebinski, R., & Timofeev, M. 1996, A&A, 306, 867
Krichbaum, T. P., Zensus, J. A., Witzel, A., et al. 1993, A&A, 274, L37
Lazarus, P., Brazier, A., Hessels, J. W. T., et al. 2015, ApJ, 812, 81
Lazio, T. J. W., Anantharamaiah, K. R., Goss, W. M., Kassim, N. E., & Cordes, J. M. 1999, ApJ, 515, 196
Lazio, T. J. W., & Cordes, J. M. 1998, ApJ, 505, 715
Liu, K., & Eatough, R. 2017, NatAs, 1, 812
Liu, K., Eatough, R. P., Wex, N., & Kramer, M. 2014, MNRAS, 445, 3115
Liu, K., Wex, N., Kramer, M., Cordes, J. M., & Lazio, T. J. W. 2012, ApJ, 747, 1

Liu, K., Young, A., Wharton, R., et al. 2019, ApJL, 885, L10
Lo, K. Y., Backer, D. C., Kellermann, K. I., et al. 1993, Natur, 362, 38
Löhmer, O., Jessner, A., Kramer, M., Wielebinski, R., & Maron, O. 2008, A&A, 480, 623
Lorimer, D. R., & Kramer, M. 2005, Handbook of Pulsar Astronomy (Cambridge: Cambridge Univ. Press)
Lu, R.-S., Krichbaum, T. P., Roy, A. L., et al. 2018, ApJ, 859, 60
Lyutikov, M. 2013, MNRAS, 431, 2580
Macquart, J., Kanekar, N., Frail, D. A., & Ransom, S. M. 2010, ApJ, 715, 939
Macquart, J.-P., & Kanekar, N. 2015, ApJ, 805, 172
Manchester, R. N., Hobbs, G. B., Teoh, A., & Hobbs, M. 2005, AJ, 129, 1993
Maron, O., Kijak, J., Kramer, M., & Wielebinski, R. 2000, in IAU Coll. 177, Pulsar Astronomy—2000 and Beyond, ed. M. Kramer, N. Wex, & R. Wielebinski (San Francisco, CA: ASP), 227
Matthews, L. D., Crew, G. B., Doeleman, S. S., et al. 2018, PASP, 130, 015002
Michel, F. C. 1982, RvMP, 54, 1
Mori, K., Gotthelf, E. V., Zhang, S., et al. 2013, ApJL, 770, L23
Morris, D., Kramer, M., Thum, C., et al. 1997, A&A, 322, L17
Pearlman, A. B., Majid, W. A., Prince, T. A., Kocz, J., & Horiuchi, S. 2018, ApJ, 866, 160
Petroff, E., Barr, E. D., Jameson, A., et al. 2016, PASA, 33, e045
Pfahl, E., & Loeb, A. 2004, ApJ, 615, 253
Plewa, P. M., Gillessen, S., Eisenhauer, F., et al. 2015, MNRAS, 453, 3234
Psaltis, D., Wex, N., & Kramer, M. 2016, ApJ, 818, 121
Radhakrishnan, V., & Cooke, D. J. 1969, ApL, 3, 225
Ransom, S. M., Eikenberry, S. S., & Middleditch, J. 2002, AJ, 124, 1788
Rea, N., Esposito, P., Pons, J. A., et al. 2013, ApJL, 775, L34
Reich, W., Fuerst, E., Reich, P., & Reif, K. 1990, A&AS, 85, 633
Schödel, R., Ott, T., Genzel, R., et al. 2002, Natur, 419, 694
Sieber, W., & Wielebinski, R. 1987, A&A, 177, 342
Spitler, L. G., Lee, K. J., Eatough, R. P., et al. 2014, ApJL, 780, L3
Torne, P., Desvignes, G., Eatough, R. P., et al. 2017, MNRAS, 465, 242
Torne, P., Desvignes, G., & Eatough, R. 2021, A&A, in press
Torne, P., Eatough, R. P., Karuppusamy, R., et al. 2015, MNRAS, 451, L50
Torne, P., Liu, K., Cognard, I., et al. 2020a, ATel, 14001, 1
Torne, P., Macías-Pérez, J., Ladjelate, B., et al. 2020b, A&A, 640, L2
Wex, N., & Kopeikin, S. 1999, ApJ, 513, 388
Wharton, R. S., Chatterjee, S., Cordes, J. M., et al. 2019, ApJ, 875, 143
Wharton, R. S., Chatterjee, S., Cordes, J. M., Deneva, J. S., & Lazio, T. J. W. 2012, ApJ, 753, 108
Wielebinski, R., Jessner, A., Kramer, M., & Gil, J. A. 1993, A&A, 272, L13
Wielebinski, R., Sieber, W., Graham, D. A., Hesse, H., & Schönhardt, R. E. 1972, Natur, 240, 131
Yao, J. M., Manchester, R. N., & Wang, N. 2017, MNRAS, 468, 3289
Zhang, F., Lu, Y., & Yu, Q. 2014, ApJ, 784, 106